

**Transport evidence for a magnetic-field induced ideal Weyl state in antiferromagnetic topological insulator  $\text{Mn}(\text{Bi}_{1-x}\text{Sb}_x)_2\text{Te}_4$**

Seng Huat Lee<sup>1,2</sup>, Yanglin Zhu<sup>1,2</sup>, Hemian Yi<sup>2</sup>, David Graf<sup>3</sup>, Rabindra Basnet<sup>4</sup>,  
Arash Fereidouni<sup>4</sup>, Aaron Wegner<sup>4</sup>, Yi-Fan Zhao<sup>2</sup>, Lujin Min<sup>2,5</sup>, Katrina Verlinde<sup>5</sup>,  
Jingyang He<sup>2,5</sup>, Ronald Redwing<sup>5</sup>, Hugh O. H. Churchill<sup>4</sup>, Nitin Samarth<sup>1,2</sup>, Cui-Zu Chang<sup>2</sup>,  
Jin Hu<sup>4\*</sup> and Z.Q. Mao<sup>1,2\*</sup>

<sup>1</sup>2D Crystal Consortium, Materials Research Institute, The Pennsylvania State University,  
University Park, PA 16802, USA

<sup>2</sup>Department of Physics, The Pennsylvania State University, University Park, PA 16802, USA

<sup>3</sup>National High Magnetic Field Lab, Tallahassee, FL 32310, USA

<sup>4</sup>Department of Physics, University of Arkansas, Fayetteville, AR 72701, USA

<sup>5</sup>Department of Materials Science and Engineering, The Pennsylvania State University,  
University Park, PA 16802, USA

**Since the discovery of Weyl semimetals (WSMs)<sup>1,2</sup>, there have been significant efforts to pursue ideal WSMs with all the Weyl nodes being symmetry related and not interfered with by any other bands. Although ideal WSM states have been realized in bosonic systems (*i.e.*, photonic crystals<sup>3</sup>), ideal fermionic WSMs are still lacking. In this Letter, we report transport evidence for a magnetic-field-induced ideal type-II Weyl state in the intrinsic antiferromagnetic topological insulator  $\text{Mn}(\text{Bi,Sb})_2\text{Te}_4$ <sup>4,5</sup>. At an optimal sample composition, we minimize the carrier density, thus lowering the chemical potential and realizing the**

**predicted ideal Weyl state. This is indicated by a large intrinsic anomalous Hall effect with a maximum Hall angle of 53% in the magnetic-field-driven ferromagnetic phase, a non-trivial  $\pi$  Berry phase of the cyclotron orbit, and a large positive magnetoresistance. Our results establish a promising platform for exploring the physics underlying the long-sought, ideal time-reversal symmetry breaking type-II WSM.**

\*Email: [jinhu@uark.edu](mailto:jinhu@uark.edu); [zim1@psu.edu](mailto:zim1@psu.edu)

Weyl semimetals (WSMs) have become a forefront research topic in contemporary condensed matter physics<sup>6-8</sup>. They provide model platforms for studying concepts in high-energy physics, such as the magnetic chiral anomaly effect. Additionally, they provide a means of realizing potentially useful exotic quantum states of technological relevance, *e.g.*, quantum anomalous Hall insulator<sup>9</sup>. In WSMs, singly-degenerate, linearly-dispersed bands cross at Weyl nodes in momentum space; these nodes always appear in pairs with opposite chirality and can be understood as monopole and anti-monopole of Berry flux. When the Weyl nodes are at or close to the chemical potential, their diverging Berry curvature can give rise to distinct properties such as a large intrinsic anomalous Hall effect (AHE) and an anomalous Nernst effect if time-reversal symmetry (TRS) is broken<sup>10-13</sup>. Further, the bulk-edge correspondence principle leads WSMs to possess unique surface Fermi arcs<sup>2,14,15</sup>, which can also generate exotic phenomena such as quantum oscillations<sup>16,17</sup> and a bulk quantum Hall effect through the formation of Weyl orbits<sup>18</sup>. Further understanding of Weyl fermion physics requires *ideal* WSMs in which all Weyl nodes should be symmetry related and at the same energy (at or close to the chemical potential), without interference from any other bands<sup>6-8,19</sup>. However, although ideal WSMs have been long pursued, they have not been realized experimentally so far.

All the WSMs discovered to date are *non-ideal*: the Weyl nodes in these materials are either not close to the chemical potential, or not at the same energy, or interfered with by other bands. These non-ideal WSMs can be divided into two categories: type-I and type-II WSMs. Type-I WSMs, which feature un-tilted or weakly tilted Weyl cones, can be further categorized into inversion symmetry-breaking WSMs and TRS-breaking WSMs. The inversion symmetry-breaking type-I WSM was first established in TaAs-class materials<sup>2,15,20,21</sup>, and the TRS-breaking type-I WSM was recently demonstrated in several magnetic materials, including  $\text{Co}_3\text{Sn}_2\text{S}_2$ <sup>10,11,22-</sup>

<sup>24</sup>,  $\text{Co}_2\text{MnGa}$ <sup>25,26</sup>, and  $\text{Mn}_3\text{Sn}/\text{Mn}_3\text{Ge}$ <sup>27,28</sup>. In contrast with type-I WSMs, type-II WSMs are characterized by strongly tilted Weyl cones and violate Lorentz invariance<sup>29</sup>. The inversion-symmetry-breaking type-II WSM was found in several non-magnetic materials such as  $(\text{W}/\text{Mo})\text{Te}_2$ <sup>29-33</sup> and  $\text{TaIrTe}_4$ <sup>34,35</sup>; however, the TRS-breaking type-II WSM still remains elusive.  $\text{YbMnBi}_2$  has been reported to belong to this category<sup>36</sup>, but there has been debate regarding its TRS breaking<sup>37</sup>. In this Letter, we report transport evidence for a recently-predicted, magnetic-field-induced *ideal* TRS breaking type-II Weyl state in  $\text{MnBi}_2\text{Te}_4$ <sup>4,5</sup>.

$\text{MnBi}_2\text{Te}_4$  has been established as the first intrinsic antiferromagnetic (AFM) topological insulator<sup>4,5,38</sup>. The combination of spontaneous magnetization and non-trivial band topology makes this material accessible to a variety of exotic topological quantum states in its 2D thin layers, including the quantum anomalous Hall insulator<sup>39</sup>, the axion insulator<sup>40</sup>, and the  $C = 2$  Chern insulator<sup>41</sup>. Further,  $\text{MnBi}_2\text{Te}_4$  is also predicted to host a long-sought, ideal type-II TRS breaking WSM when its AFM order is switched to FM order by a magnetic field<sup>4,5</sup>. Theoretical studies show that the interlayer hybridization, combined with the protection of  $C_3$  rotational symmetry, induces the band crossings in the FM phase, resulting in a single pair of strongly tilted, type-II Weyl cones with the Weyl points at  $\sim 30$  meV above the chemical potential<sup>5</sup>. Here, we provide experimental evidence for such an ideal WSM using magnetotransport measurements in  $\text{Mn}(\text{Bi}_{1-x}\text{Sb}_x)_2\text{Te}_4$ . We achieve the ideal WSM by tuning the Sb:Bi ratio and observe the following key characteristics: a large intrinsic AHE with the anomalous Hall angle reaching a maximum value of 53%, a non-trivial Berry phase of cyclotron orbit, and a large positive MR in the magnetic-field-driven FM phase when the carrier density  $n$  is close to a minimum. All these results provide strong support for the predicted ideal Weyl state.

Earlier studies<sup>42,43</sup> of  $\text{Mn}(\text{Bi}_{1-x}\text{Sb}_x)_2\text{Te}_4$  show that the carrier density ( $n$ ) is minimized near  $x \sim 0.3$ , where the carrier type also changes from electron to hole<sup>42,43</sup>. Sb substitution for Bi also leads to striking changes in its magnetic properties<sup>42,43</sup>. Undoped  $\text{MnBi}_2\text{Te}_4$  shows two magnetic transitions upon increasing the magnetic field, *i.e.*, the AFM to canted antiferromagnetic (CAFM) transition at  $H_{c1}$  and the CAFM-to-FM transition at  $H_{c2}$ <sup>44</sup>. Both  $H_{c1}$  and  $H_{c2}$  are suppressed by increasing Sb content and tend to merge as  $x$  approaches 1<sup>43</sup>. Here, we investigate the magnetotransport properties of  $\text{Mn}(\text{Bi}_{1-x}\text{Sb}_x)_2\text{Te}_4$  under a high magnetic field (up to 35T) and seek transport evidence for the predicted type-II Weyl state by tuning the carrier density.

Single crystals of  $\text{Mn}(\text{Bi}_{1-x}\text{Sb}_x)_2\text{Te}_4$  used in this study were grown by a flux method (see Methods). From isothermal magnetization measurements at 2K (red curves in Fig. 1a), we find the evolution of magnetism of  $\text{Mn}(\text{Bi}_{1-x}\text{Sb}_x)_2\text{Te}_4$  with Sb content is consistent with the previous reports<sup>42,43</sup>. In Fig. 1a, the AFM, CAFM, and FM phases for each representative sample are color-coded. To examine how the magnetotransport properties of the FM phase evolve with  $n$ , we conducted high magnetic field Hall resistivity  $\rho_{xy}$  measurements for those representative samples, as shown in the upper panels of Fig. 1a (black curves).  $\rho_{xy}$  exhibits drastic changes with increasing Sb concentration  $x$ . First, the slope of  $\rho_{xy}$  shows negative-to-positive sign change near  $x = 0.26$ , indicating the carrier type changes to hole from electron for  $x > 0.26$ . Second,  $\rho_{xy}$  exhibits linear magnetic field dependence with small slope in the FM phases as  $x$  is not close to 0.26 (*e.g.*,  $x = 0, 0.79$  and  $1.0$ ), but non-linear field dependence with very large slopes as  $x$  approaching 0.26 (*e.g.*,  $x = 0.26(\text{I}), 0.26(\text{II})$  and  $0.39$ ), which can be seen clearly in the enlarged figures presented later (Figs. 3a and 3b). These observations suggest  $n$  is strongly reduced near the critical point  $x = 0.26$ , which is further verified by our angle-resolved photoemission spectroscopy (ARPES) measurements shown in Fig. 1b (see Methods). By increasing the Sb-content, a dramatic shift in

chemical potential  $\mu$  is observed and  $\mu$  is tuned into the bulk gap at  $x \sim 0.26$  (Note that the  $x = 0.26(\text{I})$  and  $0.26(\text{II})$  samples shown in Figs. 1a and 1b were cut from the two different pieces of crystals from the same batch).

In previous low magnetic field transport studies,  $n$  is determined from the paramagnetic (PM) states at 30K or 300K, where  $\rho_{xy}$  displays linear magnetic field dependence<sup>42,43</sup>. Here, for samples showing linear  $\rho_{xy}$  at high magnetic fields, we can use the slope of  $\rho_{xy}$  in the FM phase to determine  $n$  and compare it with  $n$  determined from the PM state at 75K.  $n$  obtained from these two methods differs only slightly, as shown in Fig. 1c where the purple diamond and red triangle symbols, respectively, represent  $n$  extracted from the FM and PM states (see Supplementary Fig. S1 for more details). This indicates that the magnetic-field-induced magnetic transitions do not affect  $n$  remarkably. Therefore, for samples near  $x = 0.26$  whose  $\rho_{xy}$  displays non-linear field dependence, we can estimate their  $n$  in the FM phase from their  $\rho_{xy}$  data at 75K (Supplementary Fig. S2). Following the same approach, we obtained  $n$  for many other samples with various Sb contents (Fig. 1c) and thus precisely determined the critical composition where  $n$  is a minimum. As shown in Fig. 1c, the electron (hole) density is high in the undoped parent compound  $\text{MnBi}_2\text{Te}_4$  ( $\text{MnSb}_2\text{Te}_4$ ) ( $\sim 10^{20} \text{ cm}^{-3}$ ), but drastically reduced as  $x$  approaches 0.26. The carrier density of the  $x = 0.26$  sample is  $\sim 3 \times 10^{18} \text{ cm}^{-3}$ . In the  $x = 0.26$  batch samples, we actually obtained both lightly electron- and hole-doped samples with slightly different  $n$  from different pieces of single crystals (*e.g.*, the  $x = 0.26(\text{I})$  and  $0.26(\text{II})$  samples shown in Fig. 1a and 1b and the  $x = 0.26(\text{III})$  sample shown later), indicating  $\mu$  is very close to the band edge such that small variation of  $\mu$  caused by chemical inhomogeneity (which is unavoidable for doped systems) could lead to different carrier types, as demonstrated by our ARPES data shown in Fig. 1b.

In the samples with minimal  $n$ , we observed significantly enhanced transport mobility  $\mu_H$ , reaching  $1.1 \times 10^3 \text{ cm}^2/\text{Vs}$ , about two orders of magnitude larger than those of  $\text{MnBi}_2\text{Te}_4/\text{MnSb}_2\text{Te}_4$  ( $58/9.7 \text{ cm}^2/\text{Vs}$ ), as shown in Fig. 1c (blue curve). The samples with high  $\mu_H$  exhibit strong Shubnikov–de Haas (SdH) oscillations in their field-driven FM phases, as manifested by the transverse magnetoresistance MR ( $= [\rho_{xx}(H) - \rho_{xx}(H=0)]/\rho_{xx}(H=0)$ ) data presented in the bottom panel of Fig. 1a. The strongest SdH oscillations are observed in the  $x = 0.26(\text{I})$  sample, which is electron-doped with the lowest  $n$ . These observations imply the emergence of a distinct electronic state in the FM phase as  $\mu$  is tuned near the band edge.

The analyses of the SdH oscillations indeed reveal that the FM phase hosts relativistic fermions for the samples near  $x = 0.26$ . In Fig. 2a, we show the transverse MR at various temperatures for the  $x = 0.26(\text{I})$  sample, from which we can clearly see the SdH oscillations appear following the CAFM-FM transition. A single oscillation frequency of  $F = 60\text{T}$  can be resolved by Fast Fourier transform (FFT) (see Supplementary Note 1), thus Berry phases analyses can be conducted by constructing Landau level (LL) index fan diagram (*i.e.*, LL index  $N$  vs. the inverse of the magnetic field). Distinct from non-relativistic electron systems, relativistic fermions show a zeroth LL<sup>45</sup> associated with Berry phase of  $\pi$ <sup>45</sup>, leading to a phase shift in quantum oscillations. As a result, an intercept of 0.5 is expected on the  $N$ -axis by extrapolating the linear fit to the LL fan diagram. Note that we construct the fan diagram with integer LL indices being assigned to the minimal density of state at the Fermi level ( $\text{DOS}(E_F)$ ). Since SdH oscillations originate from oscillating scattering rate, conductivity should reach maxima at the minimal  $\text{DOS}(E_F)$  where integer LL indices should be assigned<sup>19</sup> (see Methods). As shown in Fig. 2b, we derived oscillatory conductivity  $\sigma_{xx}^{osc}$  for the  $x = 0.26(\text{I})$  and 0.39 samples via inverting the resistivity

tensor ( $\sigma_{xx} = \frac{\rho_{xx}}{\rho_{xx}^2 + \rho_{xy}^2}$ ) and subtracting the non-oscillatory background. Following the above

LL index definition, we plot the LL fan diagram in Fig. 2c. The linear fits yield intercepts of  $0.48 \pm 0.03$  and  $0.64 \pm 0.06$  for  $x = 0.26$ (I) and 0.39 samples respectively, which correspond to the non-trivial Berry phases of  $(0.96 \pm 0.06)\pi$  and  $(1.28 \pm 0.12)\pi$ . This indicates the carriers participating in the SdH oscillations on both samples are relativistic fermions, consistent with the prediction of the magnetic-field-driven Weyl state<sup>4,5</sup>. Since MnBi<sub>2</sub>Te<sub>4</sub> has been established as a topological insulator<sup>4,5,38</sup>, one may wonder if the observed SdH oscillations are due to the topological surface states. This possibility can be ruled out by the observation of unusual temperature dependence of the SdH oscillations and its intimate coupling with the ferromagnetism, as discussed in Supplementary Note 2. Such coupling between magnetic and electronic properties is also in line with the predicted magnetic-field-driven FM Weyl state<sup>4,5</sup>.

We next show the relativistic fermion behavior manifested by the SdH oscillations is indeed associated with the predicted ideal Weyl state. In general, the hallmark of a WSM is the surface Fermi arc, which can directly be probed by ARPES. However, the Weyl state we are seeking here appears only in the magnetic-field-driven FM phase, making verification via ARPES impossible. In this case, magnetotransport measurements are the most effective approach for probing this Weyl state. As indicated above, a remarkable transport signature of a magnetic WSM with broken TRS is the large intrinsic AHE caused by the diverging Berry curvature of Weyl nodes, which is manifested by large anomalous conductivity (AHC)  $\sigma_{yx}^{AH}$  and anomalous Hall angles (AHA). Such an effect has been demonstrated in recently-reported magnetic WSMs such as Co<sub>3</sub>Sn<sub>2</sub>S<sub>2</sub><sup>10,11</sup>, Co<sub>2</sub>MnGa<sup>12,46</sup> and GdPtBi<sup>13,47</sup>. In the lightly-doped Mn(Bi<sub>1-x</sub>Sb<sub>x</sub>)<sub>2</sub>Te<sub>4</sub> samples, we have indeed observed large intrinsic AHE in their CAFM and FM phases. From measured

$\rho_{xy}$  and  $\rho_{xx}$ , we can extract  $\sigma_{yx}^{AH}$  using  $\sigma_{yx}^{AH} = \sigma_{yx} - \sigma_{yx}^N$  where  $\sigma_{yx}^N$  is the normal Hall conductivity. To give an example, in Figs. 3a and 3b, we present  $\rho_{xy}$  measured at various temperatures for the  $x = 0.26$ (I) and 0.39 samples. To derive  $\sigma_{yx}^{AH}$ , we define  $\sigma_{yx}^N = \sigma_{yx}(T = 75\text{K})$ , since the  $\text{Mn}(\text{Bi}_{1-x}\text{Sb}_x)_2\text{Te}_4$  system exhibits spin fluctuations above  $T_N$  and the slope of  $\rho_{xy}$  does not become constant until 75K (see Supplementary Fig. S2). Then  $\sigma_{yx}$  at 0.7K and 75K can be calculated using  $\sigma_{yx} = \rho_{xy}/(\rho_{xx}^2 + \rho_{xy}^2)$ , as shown in the insets of Figs. 3a and 3b. The difference in  $\sigma_{yx}$  between 0.7K and 75K represents AHC  $\sigma_{yx}^{AH}$ .

Fig. 3c shows the  $\sigma_{yx}^{AH}$  data of several representative samples. In contrast with heavily electron-doped (*e.g.*  $x = 0$ ) and hole-doped (*e.g.*  $x = 0.79$ ) samples which show relatively small, weakly magnetic-field-dependent  $\sigma_{yx}^{AH}$ , some lightly doped samples with  $x = 0.26$  show large and strongly magnetic-field-dependent  $\sigma_{yx}^{AH}$ . For instance, the  $-\sigma_{yx}^{AH}$  of the  $x = 0.26$ (I) sample [which is lightly electron-doped and exhibits the strong SdH oscillations (Fig. 2a)] sharply increases with magnetic field in the CAFM and reach a maximal value of  $95 (\Omega \cdot \text{cm})^{-1}$  near the CAFM-to-FM transition (see the 2<sup>nd</sup> panel from left in Fig. 3c). The lightly hole-doped samples from the same  $x = 0.26$  batch display even more unusual behavior: the  $x = 0.26$  (II) sample with the lowest hole density has very small  $\sigma_{yx}^{AH}$ , while in the  $x = 0.26$  (III) sample with slightly higher hole density, its  $\sigma_{yx}^{AH}$  varies drastically with the magnetic field, showing a sign reversal at a magnetic field between  $H_{c1}$  and  $H_{c2}$  and maximal absolute values of  $173/158 (\Omega \cdot \text{cm})^{-1}$  at  $H_{c1}/H_{c2}$ . Note that all these three samples are from the same batch and have almost the same isothermal-magnetization  $M(H)$ . The strong sample dependence of  $\sigma_{yx}^{AH}(H)$  among them suggests that their AHE is intrinsic and not coupled with magnetization. Since  $\sigma_{yx}^{AH}$  corresponds to the integration of Berry curvature for an intrinsic AHE, the strong sample dependence of  $\sigma_{yx}^{AH}$  observed here is most likely due to the fact

that a small variation of  $\mu$  caused by chemical inhomogeneity can lead to a small shift of Weyl nodes with respect to the FL, which could cause a large change of Berry curvature. The possible origin of small  $\sigma_{yx}^{AH}$  for the  $x = 0.26$  (II) sample is that type-II Weyl nodes always appear at the crossing points of electron and hole pockets, and the Berry curvature of these two pockets may cancel each other in this sample, leading to a small net Berry curvature. In addition, our observation of the striking variation of  $\sigma_{yx}^{AH}$  with magnetic field suggests the Weyl nodes may shift in the momentum space with an increasing magnetic field and start to be accessible in the CAFM phase of lightly doped samples. Further understanding of this result requires theoretical studies.

To further examine the evolution of the AHE with the carrier density  $n$ , we have converted  $\sigma_{yx}^{AH}$  to anomalous Hall angle ( $\theta_{yx}^{AH}$ , defined as  $\sigma_{yx}^{AH}/\sigma_{xx}$ ) and plot the maximal  $\theta_{yx}^{AH}$  in the FM phase at  $T = 2$  K as a function of  $n$  in Fig. 3d. For those samples measured only up to 14T, we take their  $\theta_{yx}^{AH}$  values at 14T if their AHAs do not reach maxima (see Supplementary Fig. S3). As shown in Fig. 3d, AHA increases with reducing  $n$ , reaching a maximum of 53% in a lightly hole-doped sample, comparable or larger than those of recently-discovered magnetic WSMs such as  $\text{Co}_3\text{Sn}_2\text{S}_2$  (~20%)<sup>11</sup>,  $\text{Co}_2\text{MnGa}$  (~12%)<sup>12</sup> and  $(\text{Gd/Tb})\text{PtBi}$  (~16-38%)<sup>13,47,48</sup>. Such a large  $\theta_{yx}^{AH}$  in the sample with minimal  $n$  is not only consistent with the prediction of ideal Weyl state for  $\text{MnBi}_2\text{Te}_4$ <sup>4,5</sup>, but also implies that the Weyl nodes are near the FL only when the system is lightly electron/hole-doped.

In general, signatures of a Weyl state can also be probed from MR. The chiral anomaly, manifested by negative longitudinal magnetoresistance (LMR), is usually expected for a WSM<sup>49,50</sup>. However, in  $\text{Mn}(\text{Bi}_{1-x}\text{Sb}_x)_2\text{Te}_4$ , it is hard to distinguish the negative LMR due to the chiral anomaly from other sources of negative LMR, such as the suppression of spin scattering under magnetic

fields in both CAFM and FM phases<sup>44</sup>. The other factor which prevents the clear observation of the chiral anomaly effect is that the lightly doped samples near  $x = 0.26$  exhibit a large positive MR component, which likely overwhelms the negative LMR (we discuss this below). In Fig. 4, we present transverse (Figs. 4a and 4b) and longitudinal (Fig. 4c and 4d) magnetoresistance for both heavily and lightly doped samples. All heavily electron/hole-doped samples exhibit negative magnetoresistance arising from spin flip/flop transitions, with a maximum magnitude of  $\sim 25\%$  for  $\text{MnSb}_2\text{Te}_4$  (Figs. 4a and 4c), suggesting that the transport in these samples is dominated by spin scattering. In contrast, the lightly doped samples exhibit large positive magnetoresistance (Figs. 4b and 4d). In particular, the sample showing the largest  $\theta_{yx}^{AH}$  (53%) exhibits fairly large positive MR, reaching  $\sim 228\%$  for  $H \perp I$  at 14T and  $\sim 33\%$  for  $H // I$  at 9T and 2K (Figs. 4b and 4d). In lightly electron-doped samples, the positive magnetoresistance component is relatively smaller and competes with the negative magnetoresistance due to spin scattering suppression, resulting in very unusual magnetic field dependence in the transverse magnetoresistance between  $H_{c1}$  and  $H_{c2}$  (Fig. 4b). Moreover, a large anisotropy is also observed between transverse and longitudinal magnetoresistance in lightly doped samples. All these observations clearly indicate the scattering mechanism has changed essentially when  $n$  is tuned to be close to a minimum. The large positive magnetoresistance observed in the lightly doped samples is also consistent with a Weyl state, since high mobility of Weyl fermions is generally expected to result in large positive magnetoresistance<sup>19</sup>. Such an effect is observable only when  $\mu$  is tuned near the Weyl nodes, which is exactly the scenario revealed in our experiments.

All lightly electron/hole-doped samples shown in Figs. 4b, 4d, and Fig. 3d are obtained from the same batch with  $x = 0.26$ . As seen in Fig. 4b, all these samples have a very small variation in  $n$  and similar  $H_{c1}$  and  $H_{c2}$ . However, their transverse magnetoresistance and  $\theta_{yx}^{AH}$  change

drastically. Such unusual behavior can be well understood in light of a type-II Weyl state for which Weyl fermion behavior becomes prominent only when the Weyl node are at or near the Fermi level. This is consistent with the prior work on type-II WSM  $\text{WTe}_2$ , where the Weyl fermion properties are sensitive to the chemical potential tuned by gating<sup>51,52</sup>.

In summary, by tuning the chemical potential via Sb substitution for Bi in  $\text{Mn}(\text{Bi}_{1-x}\text{Sb}_x)_2\text{Te}_4$ , we obtained lightly electron- and hole-doped samples with significantly enhanced carrier mobility; the carrier density in these samples are two orders of magnitudes less than those of parent compounds. The magnetic field-driven FM phases in these samples exhibit magnetotransport properties distinct from those of heavily doped samples, including large intrinsic AHE, strong SdH oscillations, non-trivial Berry phase of cyclotron orbit and large anisotropic positive magnetoresistance. All these results point to the predicted ideal Weyl state in the FM phase of  $\text{MnBi}_2\text{Te}_4$ . Our findings establish a promising platform for exploring novel physics of the long-sought, ideal TRS breaking type-II WSMs.

## Methods

### Sample preparation and measurements

Single crystals of  $\text{Mn}(\text{Bi}_{1-x}\text{Sb}_x)_2\text{Te}_4$  with  $x$  from 0 to 1 were grown by a self-flux method as previously reported<sup>53</sup>. The mixtures of high purity manganese powder (99.95%), antimony shot (99.9999%), bismuth shot (99.999%) and tellurium ingot (99.9999+%) with the molar ratio of  $\text{Mn}:\text{Sb}:\text{Bi}:\text{Te} = 1:5x:5(1-x):16$  were loaded into an alumina crucible and sealed in evacuated quartz tubes. The mixtures were heated up to 900°C for 12 hours to promote homogeneous melting and slowly cooled down (1.5°C/hour) to a temperature within the 590°C - 630°C range (depending on

$x$ ), followed by centrifugation to remove excess flux. Higher temperatures were used for the samples with higher Sb content to avoid the formation of  $\text{Sb}_2\text{Te}_3$  (melting point  $\sim 620^\circ\text{C}$ ). Soft, plate-like single crystals up to  $10\times 5\text{ mm}^2$  can be obtained.

The phase of single crystals is checked by x-ray diffraction. As shown in Supplementary Fig. S4, the sharp  $(00L)$  x-ray diffraction peaks, which show only small high angle shift from  $\text{MnBi}_2\text{Te}_4$  to  $\text{MnSb}_2\text{Te}_4$ , demonstrate the excellent crystallinity and the formation of the desired crystal structure with the stacking of Te-(Bi/Sb)-Te-Mn-Te-(Bi/Sb)-Te septuple layers in our single crystal samples. The composition analyses by energy-dispersive x-ray spectroscopy (EDS) show the actual Sb content  $x$  deviating from the nominal composition. In this paper, we used the measured Sb content  $x$ .

The low magnetic field magnetotransport and magnetization measurements were performed using a commercial Physical Property Measurement System (PPMS, Quantum Design, 2K/9T). The high magnetic field transport measurements were carried out using the 31T and the 35T resistive magnets at the NHMFL in Tallahassee. Standard four-probe samples are used for magnetotransport. The ARPES measurements were carried out at room temperature. The photoelectrons are excited by an unpolarized He- $I_\alpha$  light ( $\sim 21.218\text{ eV}$ ), and two analyzers (Scientia R3000 and DA30L) were used.

### **To assign LL indices for SdH oscillation**

To obtain the correct Berry phase using the LL fan diagram, integer LL indices should be assigned when Fermi energy lies between LLs, *i.e.*, at the minimal  $\text{DOS}(E_F)^{54}$ . It should be emphasized that this general principle manifests differently in quantum Hall effect and SdH effect.

In a quantum Hall system, minimal  $\text{DOS}(E_F)$  occurs at the quantized Hall plateaus where both longitudinal conductance and resistance reaches zero. The integer LL indices should be assigned in this state. However, as discussed in Ref. <sup>19</sup>, the situation becomes different for SdH oscillation. Distinct from the *non-local* transport in a 2D quantum Hall system where the edge conduction channels are dominated, the resistance or conductance in conventional *diffusive* systems are governed by scattering. According to the transport theory, the scattering probability is proportional to the number of available states that electron can be scattered into<sup>55,56</sup>; thus, it oscillates in concert with the oscillations of  $\text{DOS}(E_F)$  and gives rise to SdH oscillations<sup>57,58</sup>, leading conductivity to maxima at the minimal  $\text{DOS}(E_F)$ , where the scattering rate is minimized. Therefore, the integer LL indices, which correspond to minimal  $\text{DOS}(E_F)$ , should be assigned to conductivity maxima in the SdH effect. This approach has been verified in the nodal-line semimetal ZrSiS from the comparison between the SdH and the dHvA effects<sup>59</sup>.

## REFERENCES

- 1 Huang, S.-M. *et al.* A Weyl Fermion semimetal with surface Fermi arcs in the transition metal monophosphide TaAs class. *Nat Commun* **6**, 7373 (2015).
- 2 Weng, H., Fang, C., Fang, Z., Bernevig, B. A. & Dai, X. Weyl Semimetal Phase in Noncentrosymmetric Transition-Metal Monophosphides. *Physical Review X* **5**, 011029 (2015).
- 3 Yang, B. *et al.* Ideal Weyl points and helicoid surface states in artificial photonic crystal structures. *Science* **359**, 1013-1016 (2018).
- 4 Zhang, D. *et al.* Topological Axion States in the Magnetic Insulator  $\text{MnBi}_2\text{Te}_4$  with the Quantized Magnetoelectric Effect. *Physical Review Letters* **122**, 206401 (2019).
- 5 Li, J. *et al.* Intrinsic magnetic topological insulators in van der Waals layered  $\text{MnBi}_2\text{Te}_4$ -family materials. *Science Advances* **5**, eaaw5685 (2019).
- 6 Yan, B. & Felser, C. Topological Materials: Weyl Semimetals. *Annual Review of Condensed Matter Physics* **8**, 337-354 (2017).
- 7 Armitage, N. P., Mele, E. J. & Vishwanath, A. Weyl and Dirac semimetals in three-dimensional solids. *Reviews of Modern Physics* **90**, 015001 (2018).
- 8 Bernevig, A., Weng, H., Fang, Z. & Dai, X. Recent Progress in the Study of Topological Semimetals. *Journal of the Physical Society of Japan* **87**, 041001 (2018).
- 9 Xu, G., Weng, H., Wang, Z., Dai, X. & Fang, Z. Chern Semimetal and the Quantized Anomalous Hall Effect in  $\text{HgCr}_2\text{Se}_4$ . *Physical Review Letters* **107**, 186806 (2011).
- 10 Wang, Q. *et al.* Large intrinsic anomalous Hall effect in half-metallic ferromagnet  $\text{Co}_3\text{Sn}_2\text{S}_2$  with magnetic Weyl fermions. *Nature Communications* **9**, 3681 (2018).
- 11 Liu, E. *et al.* Giant anomalous Hall effect in a ferromagnetic kagome-lattice semimetal. *Nature Physics* **14**, 1125-1131 (2018).
- 12 Sakai, A. *et al.* Giant anomalous Nernst effect and quantum-critical scaling in a ferromagnetic semimetal. *Nature Physics* **14**, 1119 (2018).
- 13 Suzuki, T. *et al.* Large anomalous Hall effect in a half-Heusler antiferromagnet. *Nat Phys* **12**, 1119-1123 (2016).
- 14 Wan, X., Turner, A. M., Vishwanath, A. & Savrasov, S. Y. Topological semimetal and Fermi-arc surface states in the electronic structure of pyrochlore iridates. *Physical Review B* **83**, 205101 (2011).
- 15 Xu, S.-Y. *et al.* Discovery of a Weyl Fermion semimetal and topological Fermi arcs. *Science* **349**, 613-617 (2015).
- 16 Potter, A. C., Kimchi, I. & Vishwanath, A. Quantum oscillations from surface Fermi arcs in Weyl and Dirac semimetals. *Nat Commun* **5**, 5161 (2014).
- 17 Moll, P. J. W. *et al.* Transport evidence for Fermi-arc-mediated chirality transfer in the Dirac semimetal  $\text{Cd}_3\text{As}_2$ . *Nature* **535**, 266-270 (2016).
- 18 Zhang, C. *et al.* Quantum Hall effect based on Weyl orbits in  $\text{Cd}_3\text{As}_2$ . *Nature* **565**, 331-336 (2019).
- 19 Hu, J., Xu, S.-Y., Ni, N. & Mao, Z. Transport of Topological Semimetals. *Annual Review of Materials Research* **49**, 207-252 (2019).
- 20 Lv, B. Q. *et al.* Experimental Discovery of Weyl Semimetal TaAs. *Phys. Rev. X* **5**, 031013 (2015).

- 21 Yang, L. X. *et al.* Weyl semimetal phase in the non-centrosymmetric compound TaAs. *Nat Phys* **11**, 728-732 (2015).
- 22 Xu, Q. *et al.* Topological surface Fermi arcs in the magnetic Weyl semimetal  $\text{Co}_3\text{Sn}_2\text{S}_2$ . *Physical Review B* **97**, 235416 (2018).
- 23 Liu, D. F. *et al.* Magnetic Weyl semimetal phase in a Kagomé crystal. *Science* **365**, 1282-1285 (2019).
- 24 Morali, N. *et al.* Fermi-arc diversity on surface terminations of the magnetic Weyl semimetal  $\text{Co}_3\text{Sn}_2\text{S}_2$ . *Science* **365**, 1286-1291 (2019).
- 25 Wang, Z. *et al.* Time-Reversal-Breaking Weyl Fermions in Magnetic Heusler Alloys. *Physical Review Letters* **117**, 236401 (2016).
- 26 Belopolski, I. *et al.* Discovery of topological Weyl fermion lines and drumhead surface states in a room temperature magnet. *Science* **365**, 1278-1281 (2019).
- 27 Kuroda, K. *et al.* Evidence for magnetic Weyl fermions in a correlated metal. *Nat Mater* **16**, 1090–1095 (2017).
- 28 Hao, Y. *et al.* Topological Weyl semimetals in the chiral antiferromagnetic materials  $\text{Mn}_3\text{Ge}$  and  $\text{Mn}_3\text{Sn}$ . *New Journal of Physics* **19**, 015008 (2017).
- 29 Soluyanov, A. A. *et al.* Type-II Weyl semimetals. *Nature* **527**, 495-498 (2015).
- 30 Belopolski, I. *et al.* Discovery of a new type of topological Weyl fermion semimetal state in  $\text{Mo}_x\text{W}_{1-x}\text{Te}_2$ . *Nature Communications* **7**, 13643 (2016).
- 31 Huang, L. *et al.* Spectroscopic evidence for a type II Weyl semimetallic state in  $\text{MoTe}_2$ . *Nat. Mater.* **15**, 1155-1160 (2016).
- 32 Deng, K. *et al.* Experimental observation of topological Fermi arcs in type-II Weyl semimetal  $\text{MoTe}_2$ . *Nat. Phys.* **12**, 1105-1110 (2016).
- 33 Wang, C. *et al.* Observation of Fermi arc and its connection with bulk states in the candidate type-II Weyl semimetal  $\text{WTe}_2$ . *Physical Review B* **94**, 241119 (2016).
- 34 Koepernik, K. *et al.*  $\text{TaIrTe}_4$ : A ternary type-II Weyl semimetal. *Physical Review B* **93**, 201101 (2016).
- 35 Belopolski, I. *et al.* Signatures of a time-reversal symmetric Weyl semimetal with only four Weyl points. *Nature Communications* **8**, 942 (2017).
- 36 Borisenko, S. *et al.* Time-Reversal Symmetry Breaking Type-II Weyl State in  $\text{YbMnBi}_2$ . *Nature Communications* **10**, 3424 (2019).
- 37 Soh, J.-R. *et al.* Magnetic structure and excitations of the topological semimetal  $\text{YbMnBi}_2$ . *Physical Review B* **100**, 144431 (2019).
- 38 Otrokov, M. M. *et al.* Prediction and observation of an antiferromagnetic topological insulator. *Nature* **576**, 416-422 (2019).
- 39 Deng, Y. *et al.* Quantum anomalous Hall effect in intrinsic magnetic topological insulator  $\text{MnBi}_2\text{Te}_4$ . *Science*, eaax8156 (2020).
- 40 Liu, C. *et al.* Robust axion insulator and Chern insulator phases in a two-dimensional antiferromagnetic topological insulator. *Nature Materials* (2020).
- 41 Ge, J. *et al.* High-Chern-Number and High-Temperature Quantum Hall Effect without Landau Levels. arXiv:1907.09947 (2019).
- 42 Chen, B. *et al.* Intrinsic magnetic topological insulator phases in the Sb doped  $\text{MnBi}_2\text{Te}_4$  bulks and thin flakes. *Nature Communications* **10**, 4469 (2019).
- 43 Yan, J. Q. *et al.* Evolution of structural, magnetic, and transport properties in  $\text{MnBi}_2-x\text{Sb}_x\text{Te}_4$ . *Physical Review B* **100**, 104409 (2019).

- 44 Lee, S. H. *et al.* Spin scattering and noncollinear spin structure-induced intrinsic anomalous Hall effect in antiferromagnetic topological insulator MnBi<sub>2</sub>Te<sub>4</sub>. *Physical Review Research* **1**, 012011 (2019).
- 45 Ando, T. Physics of Graphene: Zero-Mode Anomalies and Roles of Symmetry. *Progress of Theoretical Physics Supplement* **176**, 203-226 (2008).
- 46 Guin, S. N. *et al.* Anomalous Nernst effect beyond the magnetization scaling relation in the ferromagnetic Heusler compound Co<sub>2</sub>MnGa. *NPG Asia Materials* **11**, 16 (2019).
- 47 Shekhar, C. *et al.* Anomalous Hall effect in Weyl semimetal half-Heusler compounds RPtBi (*R* = Gd and Nd). *Proceedings of the National Academy of Sciences of the United States of America* **115**, 9140-9144 (2018).
- 48 Singha, R., Roy, S., Pariari, A., Satpati, B. & Mandal, P. Magnetotransport properties and giant anomalous Hall angle in the half-Heusler compound TbPtBi. *Physical Review B* **99**, 035110 (2019).
- 49 Jho, Y.-S. & Kim, K.-S. Interplay between interaction and chiral anomaly: Anisotropy in the electrical resistivity of interacting Weyl metals. *Physical Review B* **87**, 205133 (2013).
- 50 Son, D. T. & Spivak, B. Z. Chiral anomaly and classical negative magnetoresistance of Weyl metals. *Physical Review B* **88**, 104412 (2013).
- 51 Wang, Y. *et al.* Gate-tunable negative longitudinal magnetoresistance in the predicted type-II Weyl semimetal WTe<sub>2</sub>. *Nature Communications* **7**, 13142 (2016).
- 52 Fatemi, V. *et al.* Magnetoresistance and quantum oscillations of an electrostatically tuned semimetal-to-metal transition in ultrathin WTe<sub>2</sub>. *Physical Review B* **95**, 041410 (2017).
- 53 Yan, J. Q. *et al.* Crystal growth and magnetic structure of MnBi<sub>2</sub>Te<sub>4</sub>. *Phys. Rev. Mater.* **3**, 8 (2019).
- 54 Ando, Y. Topological Insulator Materials. *Journal of the Physical Society of Japan* **82**, 102001 (2013).
- 55 Pippard, A. B. *The Dynamics of Conduction Electrons*. (Gordon and Breach, 1965).
- 56 Pippard, A. B. *Magnetoresistance in Metals*. (Cambridge University Press, 1989).
- 57 Shoenberg, D. *Magnetic Oscillations in Metals*. (Cambridge Univ. Press, 1984).
- 58 Kartsovnik, M. V. High Magnetic Fields: A Tool for Studying Electronic Properties of Layered Organic Metals. *Chemical Reviews* **104**, 5737-5782 (2004).
- 59 Hu, J. *et al.* Nearly massless Dirac fermions and strong Zeeman splitting in the nodal-line semimetal ZrSiS probed by de Haas-van Alphen quantum oscillations. *Physical Review B* **96**, 045127 (2017).

### Acknowledgments:

**Funding:** The study is based upon research conducted at The Pennsylvania State University Two-Dimensional Crystal Consortium–Materials Innovation Platform (2DCC-MIP), which is supported by NSF cooperative agreement DMR 1539916. Z.Q.M. acknowledges the support from the US National Science Foundation under grant DMR1707502. J.H. acknowledges the US

Department of Energy (DOE), Office of Science, Basic Energy Sciences program under Award No. DE-SC0019467 for the support of magnetization, quantum oscillation, and 31T high field transport measurements. The work at the National High Magnetic Field Laboratory is supported by the NSF Cooperative Agreement No. DMR 1157490 and the State of Florida.

## Figures Captions

**Fig. 1| Evolution of magnetic and electronic properties in  $\text{Mn}(\text{Bi}_{1-x}\text{Sb}_x)_2\text{Te}_4$ .** **a**, Magnetic field dependence of Hall resistivity  $\rho_{xy}$  and magnetization  $M$  (upper panel), and magnetoresistance (lower panel) of various  $\text{Mn}(\text{Bi}_{1-x}\text{Sb}_x)_2\text{Te}_4$  samples. All measurements were performed at  $T = 2\text{K}$  except for  $x = 0.26$  and  $0.29$  samples, for which the magnetotransport data were taken at  $0.7\text{K}$ . The carrier density and type for each sample are labeled on the top. The rose, blue, and orange regions indicate the AFM, CAFM, and FM phase regions determined by magnetization. **b**, ARPES band spectra measured on the samples with  $x = 0.26(\text{I})$  (lightly electron-doped),  $0.26(\text{II})$  (chemical potential  $\mu$  inside the bulk bandgap), and  $0.52$  (hole-doped). **c**, Composition dependence of carrier density  $n$  and transport mobility  $\mu_H$  of  $\text{Mn}(\text{Bi}_{1-x}\text{Sb}_x)_2\text{Te}_4$ .  $\mu_H$  is inferred from the Hall coefficient  $R_H (= \frac{d\rho_{xy}}{d(\mu_0 H)})$  via  $\mu_H = R_H / \rho_{xx}(0)$  where  $\rho_{xx}(0)$  is the zero field longitudinal resistivity (shown in Supplementary Fig. S5). The purple diamond and red triangle represent  $n$  determined from the high-field  $\rho_{xy}(H)$  at  $T = 2\text{K}$  (FM phase) and the low-field  $\rho_{xy}(H)$  at  $75\text{K}$  (PM phase) via  $n = \frac{1}{eR_H}$ . The samples are found to be electron-doped for  $x < 0.26$  (orange region), but hole-doped for  $x > 0.26$  (green region). In the  $x = 0.26$  batch, both electron- and hole-doped samples can be found;  $n$  reaches or is close to a minimum in these samples.

**Fig. 2| Quantum oscillations in  $\text{Mn}(\text{Bi}_{1-x}\text{Sb}_x)_2\text{Te}_4$ .** **a**, Transverse magnetoresistance of the  $x = 0.26(\text{I})$  sample at various temperatures from  $T = 0.7\text{K}$  to  $75\text{K}$ . Quantum oscillations in the FM phase are clearly seen at low temperatures. **b**, Conductivity oscillations  $\sigma_{xx}^{osc}$  of the  $x = 0.26(\text{I})$  and  $0.39$  samples obtained from the tensor conversion and background subtraction. Integer LL indices

are assigned to the maximal conductivity where  $\text{DOS}(E_F)$  reaches the minimum (see Methods). **c**, LL fan diagram built from conductivity oscillations shown in (b). From the linearly extrapolated intercept  $N_0$ , the Berry phase can be extracted via  $2\pi N_0$  for a two-dimensional (2D) or quasi-2D system. The materials studied here should be quasi-2D, as demonstrated by the angular dependence of oscillation shown in Supplementary Note 1. The relatively low oscillation frequency allows for approaching very low LLs in both samples. The slopes of the fitted lines are  $61.2 \pm 0.3\text{T}$  and  $80.6 \pm 0.9\text{T}$  for  $x = 0.26(\text{I})$  and  $0.39$  samples, respectively, agreeing well with the oscillation frequencies obtained by FFT (60T and 82T, see Supplementary Note 1). This result, together with the accessibility of very low LLs, guarantees the reliability of the Berry phase obtained from LL fan diagram<sup>54</sup>.

**Fig. 3| Anomalous Hall effect in  $\text{Mn}(\text{Bi}_{1-x}\text{Sb}_x)_2\text{Te}_4$ .** **a-b**, Hall resistivity  $\rho_{xy}$  as a function of magnetic field for the (a)  $x = 0.26(\text{I})$  and (b)  $x = 0.39$  samples at various temperatures. AHE can be clearly seen in both samples. The insets show Hall conductivity  $\sigma_{xy}$  at  $T = 0.7\text{K}$  (black) and  $75\text{K}$  (orange), obtained from tensor conversion. **c**, Field dependence of AHC for the samples with  $x = 0, 0.26(\text{I}), 0.26(\text{II}), 0.26(\text{III}), 0.39,$  and  $0.79$  at  $0.7\text{K}/2\text{K}$ . **d**, The absolute value of maximal anomalous Hall angle  $|\theta_{yx}^{AH}|$  in the FM phase a function of carrier density (note that for those samples which were measured only up to 14T, we took the values of  $|\theta_{yx}^{AH}|$  at 14T if its maximal value is not reached below 14T;  $|\theta_{yx}^{AH}|$  exhibits weak field dependence above 14T, see Supplementary Fig. S3 for details). All data points are obtained at 2K, except for the  $x = 0.26(\text{I}), 0.26(\text{II})$  and  $0.39$  samples (0.7K).

**Fig. 4| Magnetoresistance of  $\text{Mn}(\text{Bi}_{1-x}\text{Sb}_x)_2\text{Te}_4$ .** **a-b**, In-plane transverse MR for (a) heavily electron/hole-doped and (b) lightly electron/hole-doped  $\text{Mn}(\text{Bi}_{1-x}\text{Sb}_x)_2\text{Te}_4$ , measured with the magnetic field perpendicular to the current (within the  $ab$ -plane). Critical fields for the AFM-to-CAF $\text{M}$  transition ( $H_{c1}$ ) and CAF $\text{M}$ -to-F $\text{M}$  transition ( $H_{c2}$ ) are labeled in (b). **c-d**, In-plane longitudinal MR for (c) heavily electron/hole-doped and (d) lightly electron/hole-doped  $\text{Mn}(\text{Bi}_{1-x}\text{Sb}_x)_2\text{Te}_4$ , measured with the in-plane magnetic field parallel to the current. All lightly doped samples are from the same batch with  $x = 0.26$ . The insets show the measurement setup.

Figure 1

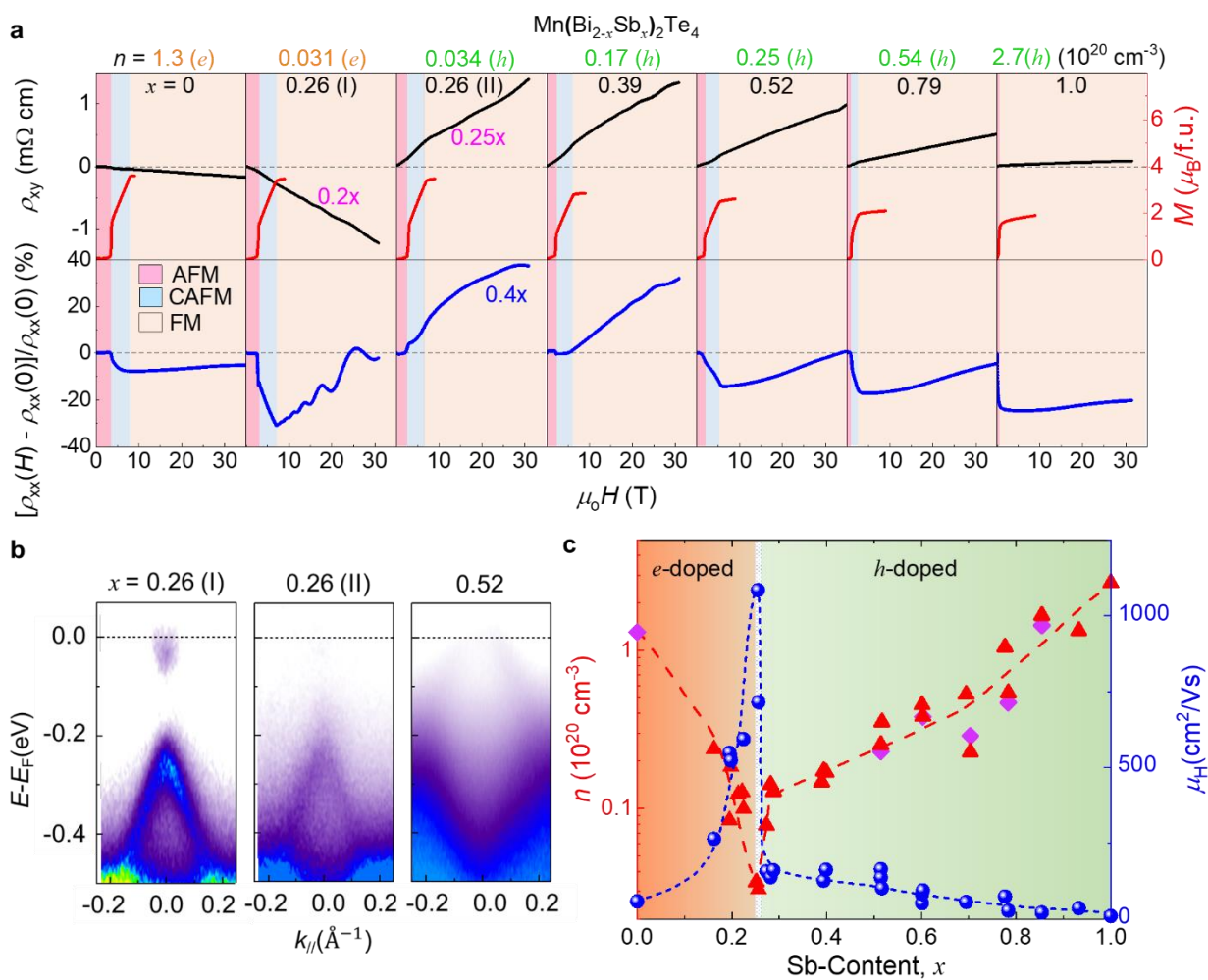


Figure 2

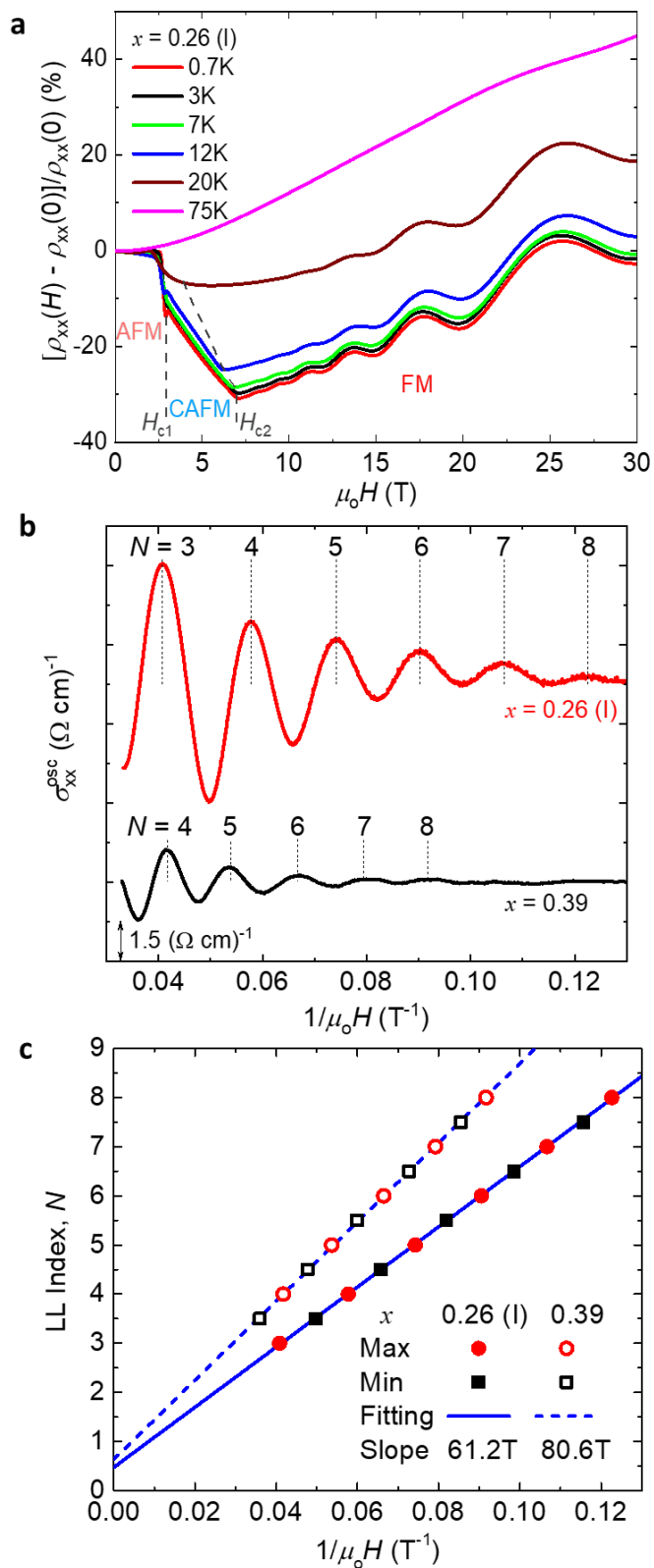


Figure 3

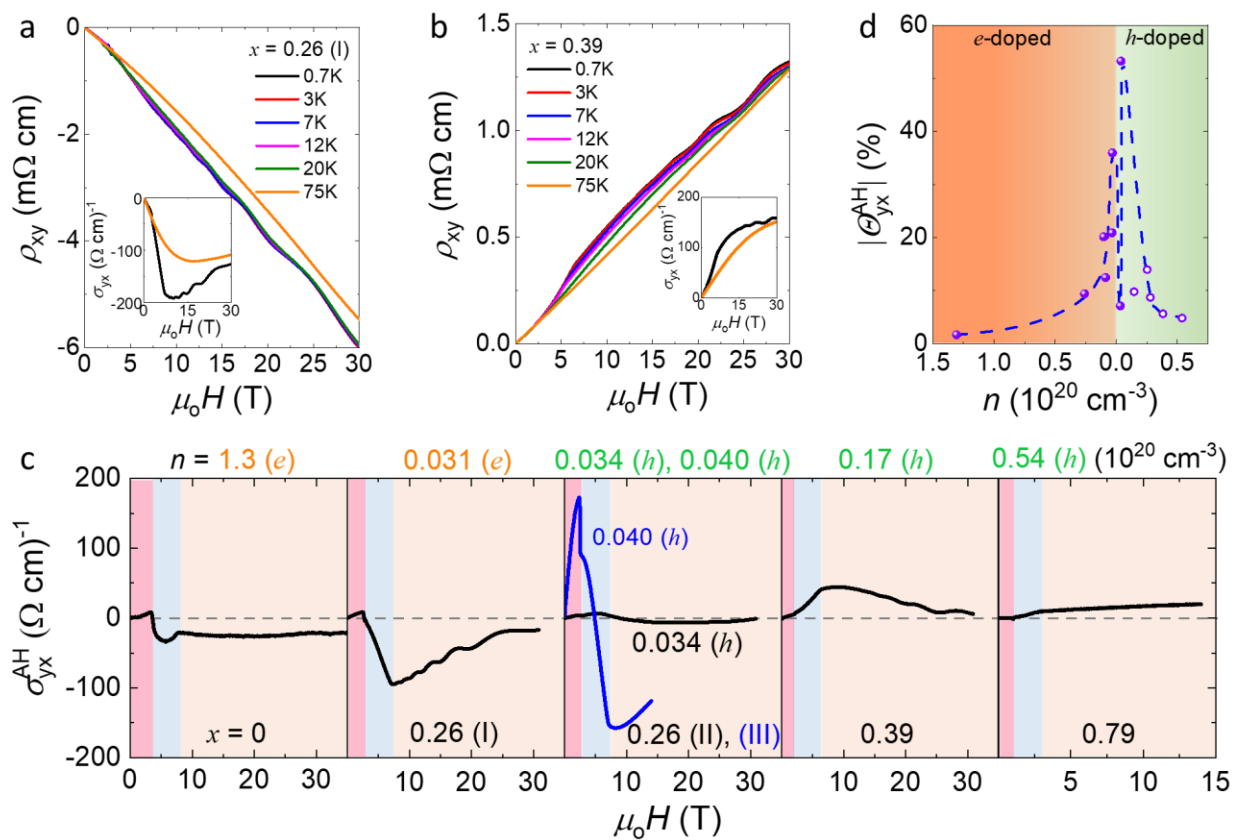


Figure 4

